

Article

X-ray Absorption Spectroscopy Investigation of Platinum–Gadolinium Thin Films with Different Stoichiometry for the Oxygen Reduction Reaction

Kim Degn Jensen ^{1,2}, Anders Filsoe Pedersen ², Eleonora Zamburlini ²,
Ifan Erfyl Lester Stephens ^{2,3}, Ib Chorkendorff ² and María Escudero-Escribano ^{1,2,*}

¹ Department of Chemistry, Nano-Science Center, University of Copenhagen, Universitetsparken 5, DK-2100 Copenhagen Ø, Denmark; kimdegn@chem.ku.dk

² Department of Physics, Surface Physics and Catalysis, Technical University of Denmark, Fysikvej, DK-2800 Lyngby, Denmark; anfil@fysik.dtu.dk (A.F.P.); eza@netcompany.com (E.Z.); i.stephens@imperial.ac.uk (I.E.L.S.); ibchork@fysik.dtu.dk (I.C.)

³ Department of Materials, Imperial College London, 2.03b, Royal School of Mines, Prince Consort Rd, London SW72AZ, UK

* Correspondence: maria.escudero@chem.ku.dk

Received: 12 June 2020; Accepted: 19 August 2020; Published: 31 August 2020



Abstract: Alloys of platinum and lanthanides present a remarkable activity for the oxygen reduction reaction—both in the form of extended surfaces and nanoparticulate catalysts. Co-sputter-deposited thin film catalysts based on platinum and gadolinium show great oxygen reduction activity improvement over pure Pt. The sputter-deposition technique represents a viable and versatile approach for investigating model catalyst systems with different compositions. In this work, co-sputtered Pt₅Gd and Pt_{7.5}Gd thin films were investigated using X-ray absorption spectroscopy as well as standardized electrochemical techniques. These investigations revealed the importance of forming alloys with specific stoichiometry, supporting the need of forming compressively strained Pt overlayers in order to achieve optimum catalytic performances.

Keywords: X-ray absorption spectroscopy; electrocatalysis; Pt alloys; thin films; co-sputter deposition; oxygen reduction reaction

1. Introduction

Hydrogen-fueled energy conversion devices such as low-temperature fuel cells are expected to play a key role in the transition towards a sustainable economy [1]. Pt-based electrocatalysts hold great promise for the oxygen reduction reaction (ORR) in proton exchange membrane fuel cells (PEMFCs) [1]. However, a high loading of 0.2 mg_{Pt}/cm² is required at the cathode [2], where the ORR takes place. Since the amount of Pt available is very scarce [3], we need to reduce the Pt-loading at the cathode, while enhancing the ORR catalytic activity. Substantial progress [4] has been made in recent years to improve the sluggish ORR kinetics [5]. This rapidly progressing research field has resulted in a wide range of intricate principles for the rational design of Pt-based oxygen electroreduction nanocatalysts [6–11].

Elucidating the factors governing ORR is essential to design more efficient electrocatalysts. The ORR activity on Pt-based catalysts follows a Sabatier volcano relationship with the binding energy of the oxygen-containing reaction intermediates, e.g., OH. This has been thoroughly corroborated from extensive density functional theory (DFT) calculations [12,13]. These calculations show that the optimum activity value (the top of the volcano) should be achieved by an electrocatalyst which binds OH ca. 0.-eV weaker than pure Pt [13]. Design principles from a combination of model studies on well-defined electrode surfaces [14–18] and DFT calculations have facilitated the development of

tailored Pt-based bimetallic nanocatalysts [19]. Recent strategies for the rational design of enhanced electrocatalysts include tuning the electronic structure by means of Pt–Pt surface strain [6,20–22] or ligand effects [16,17], as well as controlling the generalized coordination number [23], the size of nanoparticulate catalysts [24,25], the morphology of the nanoparticles [7,10,19,26] and the utilization of noble metals through single-site optimization [11,27–30].

In earlier studies, we identified alloys of Pt and rare earth metals such as Y and Gd as active and stable electrocatalysts for ORR in acidic media [9,20–22,31,32]. The high stability and activity can be explained by the formation of a thick Pt overlayer under compressive strain—as the rare earth component is vulnerable towards dissolution and tends to leach out from the surface layer, the Pt overlayer protects it against further leaching [33]. Electronic strain effects [34] occur due to the formation of this thick Pt overlayer on top of the bulk Pt–Gd alloy and has been observed to form on both on polycrystalline Pt₅Gd [22] and Gd/Pt(111) single-crystalline electrodes [31,35]. Compressive strain of the Pt overlayer originates from a combination of so-called Kagomé layers stabilized by larger Gd atoms in the bulk Pt–Gd alloy [22,36]. Gd/Pt(111) electrode surfaces show that such strain formation leads to a weakening of the OH binding energy, resulting in improved ORR kinetics [31,35]. Notably, our work on polycrystalline Pt–lanthanide alloys shows that Pt₅Gd electrodes indeed exhibit ORR activities near the top of the Sabatier volcano [19,22]. X-ray diffraction (XRD) measurements showed that all the investigated bulk Pt₅ M (M = lanthanide) alloys exhibited a hexagonal structure [22]. Moreover, we recently investigated the structure of the active phase of Gd/Pt(111) by means of in situ synchrotron grazing incidence X-ray diffraction (GI-XRD) [35]. The compressively strained Pt overlayer forms under open-circuit conditions; the strain relaxes slightly upon repeated electrochemical cycling between 0.6 and 1.0 V vs. the reversible hydrogen electrode (RHE). Interestingly, stability measurements on Gd/Pt(111) cycling between 0.6 and 1.0 V vs. RHE show that the Pt overlayer exhibits a very stable structure when cycling in this potential range [35].

A key understanding of the structure of the active phase from our work on extended Pt–lanthanide alloys enabled the design and development of nanoparticulate Pt–Gd catalysts in the form nanoparticles [21] and thin films [37], both exhibiting enhanced ORR activity over pure Pt. Extended X-ray absorption fine structure (EXAFS) measurements on mass-selected Pt_xGd and Pt_xY nanoparticles showed that their ORR activity increased exponentially with the bulk compressive strain [21].

Investigating Pt–Gd ratios that will lead to a compressive strain of the Pt overlayer that allow the desirable weakening of the OH binding energy would be key to design and develop Pt–Gd catalysts exhibiting optimum values of both ORR activity and stability. Moreover, chemical synthesis of alloys containing metallic Gd has demonstrated exceedingly difficult due to the oxophilic nature of Gd [37]. Physical techniques such as sputtering in ultra-high vacuum (UHV) are very suitable to fabricate Pt-based thin films with different stoichiometry [37–39]. We recently investigated Pt, Pt₅Gd and Pt₃Y thin films as catalysts for the ORR [37,38], where we took specific care in ensuring that oxygen had not been incorporated into the thin films and the strained Pt overlayers were formed on top of the alloy surfaces when subjected to electrochemical testing [31,35].

Herein, insights gathered from ex situ X-ray absorption spectroscopy (XAS) measurements on Pt₅Gd and Pt_{7.5}Gd thin films both as-prepared and after electrochemistry (see Figure 1) will be presented in combination with electrochemical characterization of the co-sputtered Pt_xGd thin films. While our XAS measurements were carried out at Stanford Synchrotron Radiation Lightsource (SSRL), all the fabrication and electrochemical testing was performed at the Technical University of Denmark (DTU).

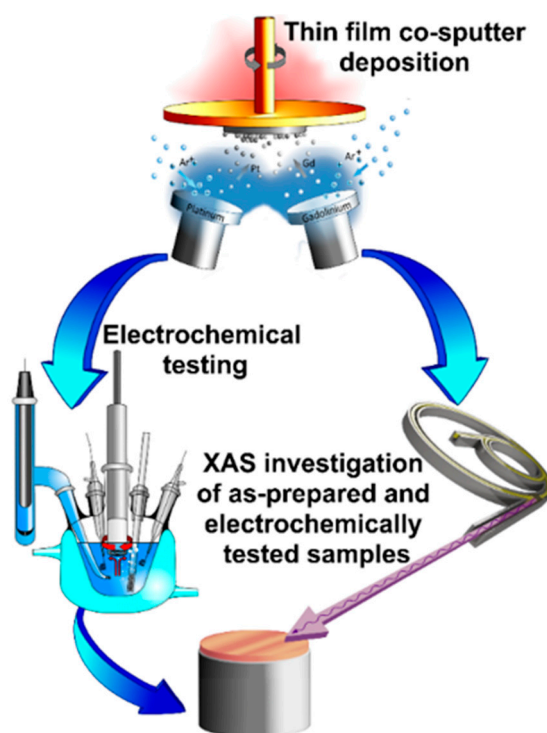


Figure 1. Illustration of the experimental methods carried out to investigate 10-nm Pt_xGd thin films. The thin films were prepared by co-sputtering [37], some of them were then subjected to electrochemical testing in a standard three-electrode setup. Both as-prepared and electrochemically tested samples were studied using X-ray absorption spectroscopy (XAS).

2. Results and Discussion

Pt_xGd thin films were produced by means of co-sputtering Pt and Gd [37]. Pt_xGd thin films form catalytically active Pt overlayers under electrochemical conditions [37,38]. To investigate the structure of the Pt overlayers, ex situ XAS was employed on 10-nm-thick Pt_xGd samples, both as-prepared and after electrochemical cycling in 0.1-M $HClO_4$, see Materials and Methods for details.

Our earlier investigations on the formation of Pt and Pt_xGd thin films [37] revealed that thin films of thicknesses <27 nm were prone to pinhole formation during sputtering. Hence, a range of thin films of ~ 50 -nm-thickness was made in parallel with the 10-nm thin films. The 50-nm thin films were the basis for the electrochemical ORR activity and stability measurements, while the 10-nm thin films were the basis for the XAS investigations. Using the small thickness films for XAS was a way of obtaining surface sensitive XAS as thicker 50-nm samples would give information on the bulk structure of the thin films. Hence, 10-nm $Pt_{7.5}Gd$ and Pt_5Gd co-sputter-deposited thin films were transferred to a N_2 -saturated 0.1-M $HClO_4$ containing three-electrode electrochemical cell (see Figure 1). Pt_xGd thin films were then cycled from 0.6 to 1.0 V vs. RHE until stable CVs were formed (see Figure 2a). By means of CO-stripping measurements and H-adsorption areas from the base CVs, we were able to estimate the roughness factor ($\Gamma_{CO/H ad.} = A_{CO/H ad.}/A$) of the thin films, where (A) designates the geometric electrode area. Although the diameter of the electrode was 5.0 mm, the outer 0.05 mm around the rim was covered by a mask. However, we neglect this small difference, corresponding to a $\sim 4\%$ smaller sputter area on the electrode (see Table 1).

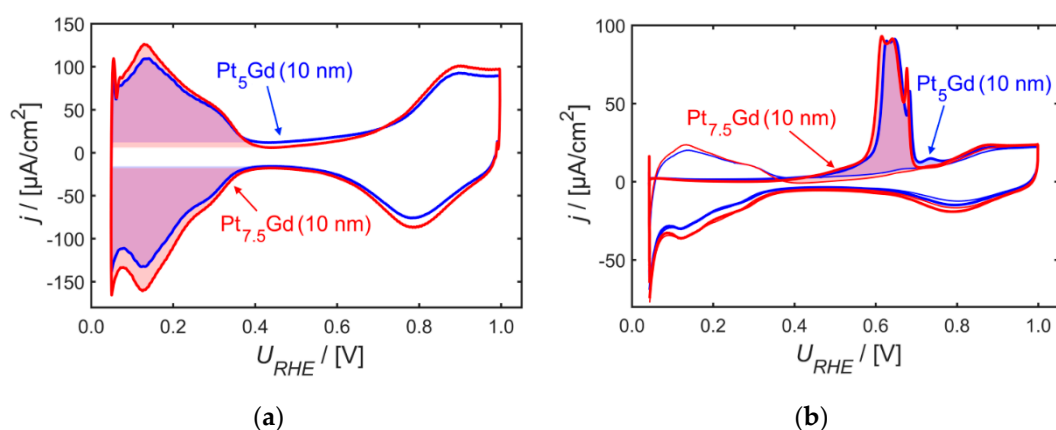


Figure 2. Cyclic voltammograms on 10 nm Pt₅Gd (blue curves) and Pt_{7.5}Gd (red curves) thin films in 0.1-M HClO₄; (a) Base cyclic voltammograms (CVs) in N₂-saturated electrolyte taken at 50 mV/s; (b) CO-stripping measurements at 10 mV/s. Sketched areas of (a,b) correspond to charge areas used for evaluating H adsorption and CO oxidation, respectively. All current densities were normalized to the geometric electrode area of ~0.196 cm².

Table 1. Fitted extended X-ray absorption fine structure (EXAFS) and electrochemical characterization data for Pt_xGd (10 nm) samples as prepared and after electrochemical conditioning, the latter denoted by “*”. All EXAFS strain data relied on a Pt foil reference measurement [21] in which a relaxed Pt–Pt bond length of 2.775 Å was established, see S.I. EXAFS data are given with ±0.01 Å. This corresponds to a strain error of about 0.4%.

Parameter	Pt _{7.5} Gd (10 nm)		Pt ₅ Gd (10 nm)	
Pt–Pt distance (Å)	2.73	2.75 *	2.69	2.73 *
Pt–Pt strain %	–1.6	–0.8 *	–3.1	–1.6 *
Gd–O distance (Å)	2.39	n.a.*	2.39	2.28 *
Pt-overlayer strain %	n.a.	–0.3 *	n.a.	–0.5 *
Q _{CO} (µC)	n.a.	162.1 *	n.a.	135.7 *
Q _{H ad.} (µC)	n.a.	97.1 *	n.a.	79.5 *
Γ _{CO}	2.4	2.5 *	2.0	2.1 *
Γ _{H ad.}	2.6	2.7 *	2.1	2.2 *

* after electrochemical cycling until stable CVs formed.

Two as-prepared and two electrochemically conditioned 10-nm-thick Pt_{7.5}Gd and Pt₅Gd thin films were then transferred to SSRL and ex situ EXAFS spectra were obtained for these four samples (see Figure 3).

EXAFS spectra at the Gd L₃ and Pt L₃ line-edges for the four 10-nm Pt_xGd samples were obtained and fitted (see S.I.). Both the electrochemical data and EXAFS results from Figures 2 and 3 are summarized in Table 1. Real-space transforms of EXAFS data can be found in Figures S1 and S2.

The results summarized in Table 1 suggest that, when the Pt_xGd thin films are formed, significant oxygen is present in the surface layer, as observed by the significant Gd–O coordination. This suggests that the oxophilic nature of Gd [37] results in a significantly oxidized surface termination (see S.I.). Moreover, the electrochemical conditioning of the thin films significantly reduces the Gd–O coordination suggesting gadolinium-oxides in the surface dissolve completely during cycling in the acidic electrolyte. Similar observations were made from earlier X-ray photoelectron spectroscopy (XPS) studies [37].

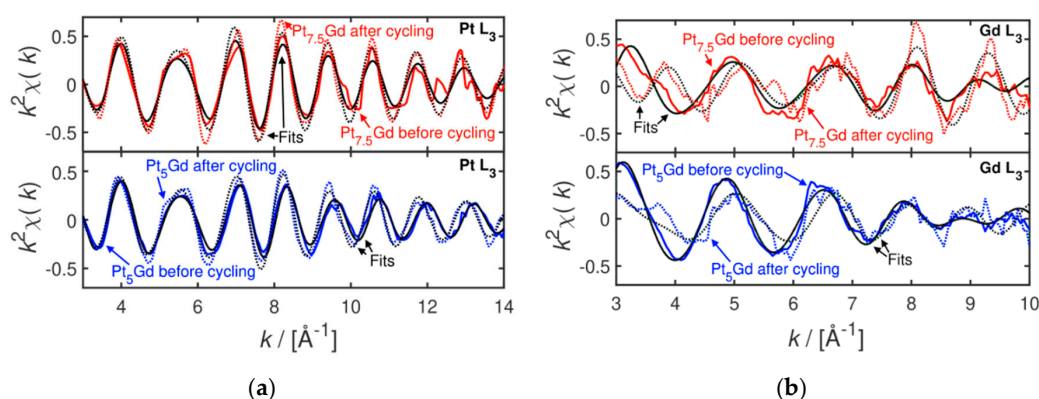


Figure 3. k^2 -weighted EXAFS oscillation function plotted vs. the wavenumber for 10-nm Pt_5Gd and $\text{Pt}_{7.5}\text{Gd}$ thin films (blue and red, respectively) both before (full lines) and after (dashed lines) electrochemical cycling; (a) Pt L_3 edge; (b) Gd L_3 edge.

As expected, the nearest Pt–Pt distance from Table 1 increases after electrochemical cycling. The Pt–Pt distance of the pure Pt overlayer lies between that of the Pt_xGd alloy and bulk Pt [36]. Thus, when the thin film is transformed from mostly alloy to part alloy and part overlayer, the average Pt–Pt distance is increased. This is also evident from the raw data in Figure 3a: In reciprocal space, the frequency increases due to longer average distances in real space. After the electrochemical cycling, a compressively strained Pt overlayer is formed from Gd leaching, in agreement with earlier studies of Pt rare-earths and lanthanide alloys [22,35,37,38]. The formation of the overlayer was supported by an additional measurement on the Pt_5Gd sample at a shallower angle (at 0.2° which increases the signal contribution from the surface), in which we observe marginally increased Pt–Pt distances.

Table 1 also shows that relatively high roughness factors are found both from H-adsorption and CO-stripping area measurements. This strongly suggests that extensive pinhole is formed due to the low thickness of 10 nm (see S.I.). Unfortunately, concluding on any compressive strain difference (seen from the Pt–Pt distance) between the $\text{Pt}_{7.5}\text{Gd}$ and Pt_5Gd sample is not straightforward, given the extensive roughness. From our earlier work on well-defined extended surfaces [22], we expect Pt_5Gd to exhibit superior ORR activity performance, as its Pt overlayer is more compressively strained than that of $\text{Pt}_{7.5}\text{Gd}$. Indeed, we recently observed that the overlayer strain on polycrystalline Pt_5Gd leads to an activity that approaches the top of the experimental volcano [22]. We note that, according to theoretical calculations [13,32], the OH weakening leading to an optimal ORR activity corresponds to a Pt overlayer under a compressive strain of ca. 3% relative to pure Pt [22].

To further correlate Pt:Gd stoichiometry with ORR activity, 50-nm-thick $\text{Pt}_{7.5}\text{Gd}$ and Pt_5Gd thin films were produced and electrochemically characterized. We must note that we carried out the electrochemical measurements on 50-nm thin films as we could not use thinner films due to the presence of pinholes and excess of under-coordinated sites associated (see Figure S3) [37]. Following earlier established electrochemical characterization procedures on Pt_5Gd thin films [37], a minimum of four samples of each composition were tested using standard rotating disk electrode (RDE) measurements in 0.1-M HClO_4 electrolyte using a three-electrode setup, as shown in Figure 1. The base CVs on Pt_xGd (50-nm) thin films before and after accelerated stability tests (see Section 3 Materials and Experimental Methods) were evaluated in conjunction with CO-stripping experiments and CVs under ORR conditions. Representative base CVs and CO oxidation can be seen in Figure 4a,b, respectively.

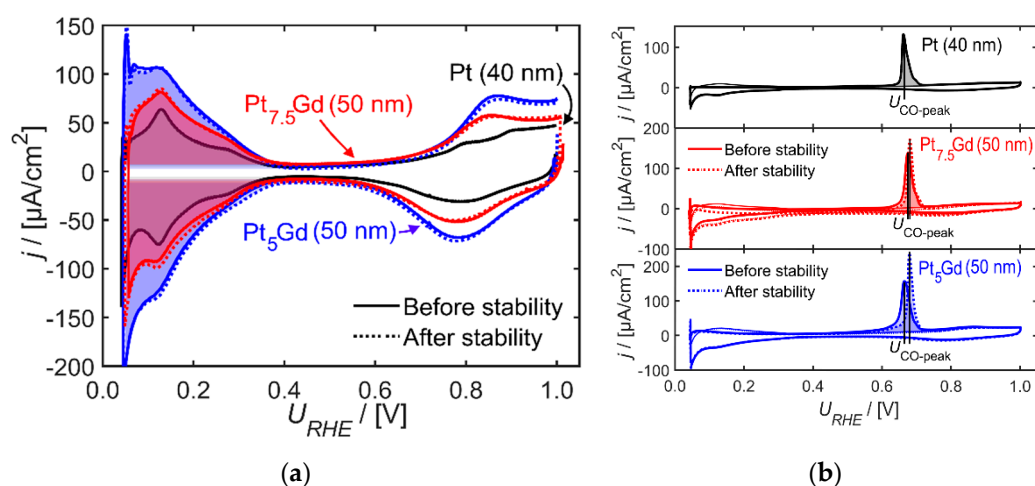


Figure 4. Electrochemical characterization and electrochemically active surface area (ECSA) determination of pure 40-nm Pt, 50-nm-thick Pt₅Gd (blue) and Pt_{7.5}Gd (red) thin films in 0.1-M HClO₄ electrolyte at room temperature before (full lines) and after stability (dashed lines) tests; (a) base CVs in N₂-saturated electrolyte at 50 mV/s and 400 rpm, with H-adsorption charge area sketched; (b) CO-stripping peaks of Pt (top) Pt_{7.5}Gd (center) and Pt₅Gd (bottom) at 10 mV/s in N₂-saturated electrolyte and 200 rpm, with CO-stripping charge area sketched. Potential of the maxima of the CO oxidation peaks is included. All current densities normalized to the geometric electrode area of ~0.196 cm².

From the base CVs in Figure 4a, it is noted that features typically associated with H and OH adsorption and desorption [16,40] do not change significantly after accelerated test. This suggests the formation of stable films under the presented electrochemical conditions. Conversely, there is a small shift in the position of the CO stripping peak. In this context, it should be noted that CO can induce Pt surface roughening/smoothing [41–43] and general reorganization [44]. The CO-stripping experiments from Figure 4b, presented in Table 2, reveals that; (i) Quite rough thin film surfaces form. (ii) Pt_{7.5}Gd thin films are less rough than Pt₅Gd thin films, likely due to the lower degree of Gd dissolution by acid leaching [35]. (iii) The potential of the maximum CO oxidation peak increases after stability tests and the $U_{\text{CO-peak}}$ value attains similar values for both the Pt₅Gd and Pt_{7.5}Gd samples, suggesting a similar structure is formed after aging.

Table 2. Electrochemical data for the 40 nm Pt as-prepared and 50 nm Pt₅Gd and Pt_{7.5}Gd thin films before and after AST. Specific activities were evaluated at 0.9 V vs. RHE and are shown both using the area derived from CO oxidation and hydrogen adsorption [37].

Parameter	Pt (40 nm) Before AST	Pt ₅ Gd (50 nm) Before AST	Pt ₅ Gd (50 nm) After AST	Pt _{7.5} Gd (50 nm) Before AST	Pt _{7.5} Gd (50 nm) Before AST
Q_{CO} (μC)	75.4 ± 7	116 ± 25	118 ± 25.5	91 ± 17	93 ± 17
$Q_{\text{H ad.}}$ (μC)	35.3 ± 4	65 ± 16	66 ± 16	55 ± 8	59 ± 9
A_{CO} (cm ²)	0.19 ± 0.04	0.33 ± 0.07	0.34 ± 0.07	0.26 ± 0.05	0.27 ± 0.05
$A_{\text{H ad.}}$ (cm ²)	0.18 ± 0.04	0.34 ± 0.08	0.35 ± 0.08	0.29 ± 0.04	0.31 ± 0.04
Γ_{CO}	1.0 ± 0.1	1.7 ± 0.4	1.8 ± 0.4	1.3 ± 0.3	1.4 ± 0.3
$\Gamma_{\text{H ad.}}$	0.9 ± 0.1	1.7 ± 0.4	1.9 ± 0.5	1.5 ± 0.2	1.6 ± 0.2
$U_{\text{CO-peak}}$ (mV)	662 ± 16	679 ± 70	672 ± 10	657 ± 13	680 ± 1
$j_{k,\text{CO}}$ (mA/cm ²)	4.7 ± 0.8	10.0 ± 3.4	9.1 ± 3.1	7.8 ± 0.6	7.3 ± 0.6
$j_{k,\text{H ad.}}$ (mA/cm ²)	4.9 ± 0.8	9.6 ± 1.9	8.3 ± 1.6	7.2 ± 0.7	6.7 ± 0.7

The ORR activity of the Pt_xGd thin films was also electrochemically evaluated. Representative anodic sweeps during ORR can be seen in Figure 5a. It should be noted that the ORR activities were evaluated using the Koutecky–Levich relation, which identifies the mass-transport corrected kinetic component (j_k) of the oxygen reduction current density (j) taking into account the diffusion limiting

current density (j_{diff}): $j_k^{-1} = j^{-1} - j_{diff}^{-1}$ [45]. The logarithm of the kinetic current density was plotted against the RHE potential to obtain a Tafel plot, as seen in Figure 5b.

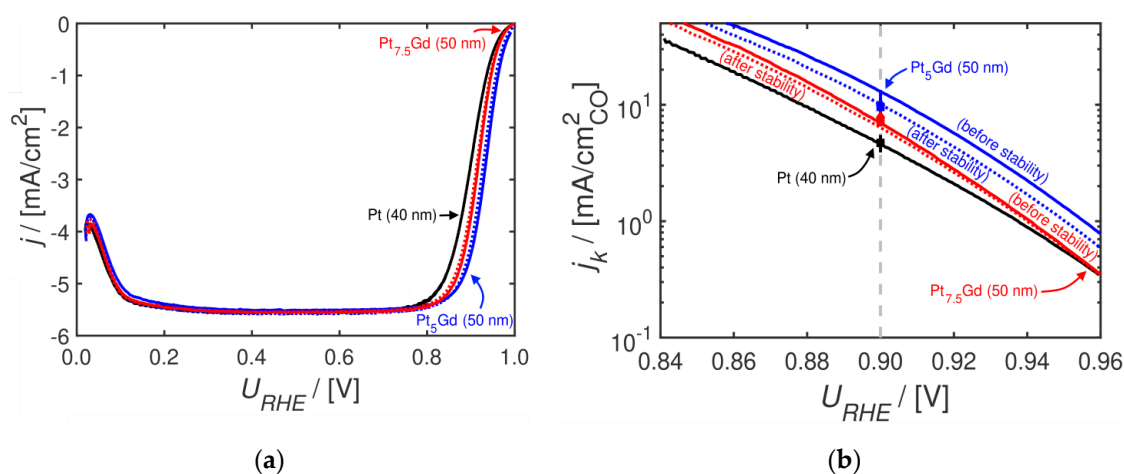


Figure 5. ORR activity plots of 40 nm Pt, 50 nm Pt₅Gd (blue) and Pt_{7.5}Gd (red) thin films in O₂-saturated 0.1-M HClO₄ electrolyte at 50 mV/s and 1600 rpm at room temperature both before (full lines) and after stability (dashed lines) tests; (a) Current density of the anodic ORR sweep using electrodes geometric area; (b) Tafel plot using the CO-oxidation area for charge density normalization, also shown is the average specific activities at 0.9 V vs. RHE (gray line) with error bars of minimum three measurements of each composition. The observed Tafel slopes were found to be very similar for all systems $\beta_{Pt_5Gd_{thin\ film}} \sim 58.1 \frac{mV}{dec.}$, $\beta_{Pt_5Gd_{poly}} \sim 55.5 \frac{mV}{dec.}$, $\beta_{Pt_{poly}} \sim 63.1 \frac{mV}{dec.}$, $\beta_{Pt_{thin\ film}} \sim 59.6 \frac{mV}{dec.}$ at 0.9 V vs. RHE, respectively.

The electrochemically active surface areas derived from the CO-stripping charges were utilized to estimate the kinetic current densities in Figure 5b, whereas current densities in Figure 4a,b and Figure 5a were normalized by the geometric electrode area of ca. 0.196 cm² [37]. From the electrochemical characterization (Figures 4 and 5) key parameters such as CO and H-adsorption charge (Q) and associated active electrodes areas (A) and roughness factors (Γ) could be extracted. Moreover, kinetic current densities for ORR and CO oxidation peak potential are summarized in Table 2. Table 2 shows that Pt₅Gd (50 nm) and Pt_{7.5}Gd (50 nm) samples present differences in ORR activity, Pt₅Gd being more active than Pt_{7.5}Gd, as expected from a higher Pt–Pt compressive overlayer strain [22].

3. Materials and Methods

3.1. Thin Film Fabrication

Pt_xGd and Pt thin films were produced by a (co)sputtering method described elsewhere [37]. A polished and clean glassy-carbon stub (HTW, $\varnothing \times h = 5 \times 4$ mm) was placed in an ultra-high vacuum system. The system base pressure was 10⁻⁹ mbar. Thin films of Pt–Gd alloys were co-sputtered atop using Ar (N5, 50 sccm) and powers of 180 W and 17–20 W for the Pt and Gd targets, respectively (Kurt–Lesker, 99.995%). The film thickness was monitored using a quartz microbalance; the deposition temperature was maintained at 300 °C.

3.2. Electrochemical Conditioning and Characterization of Pt_xGd Co-sputtered Thin Films

The co-sputtered Pt_{7.5}Gd and Pt₅Gd thin films (10-nm-thick) used for the EXAFS investigation were transferred to a N₂-saturated 0.1 M HClO₄ (Merck, Suprapur[®], 70%) containing three-electrode electrochemical cell (see Figure 1). The samples were immersed into the electrochemical cell under potential control and cycled at 50 mV/s between 0.05 and 1.00 V vs. the RHE until stable cyclic voltammograms (CVs) were obtained. The charge associated with H adsorption ($Q_{H\ ad.}$) can be used to

estimate the electrochemically active surface area (ECSA) of Pt catalysts [37,46–48]. Once stable CVs had formed, CO-stripping measurements were conducted at 10 mV/s [37,49]. The CO-stripping procedure consisted of sample being cycled twice in Ar-saturated electrolyte at 10 mV/s. Then, the electrode was maintained at 0.05 V vs. RHE while bubbling CO for 2 min, saturating the electrode surface. The electrode potential was maintained at 0.05 V vs. RHE for 15 min while bubbling Ar gas purging the remaining CO from the electrolyte. This allowed CO to be adsorbed on the electrode surface, while allowing sufficient time for residual CO to be purged from the cell. The potential was then swept between 0.05 V and 1.00 V vs. RHE at 10 mV/s. The CO oxidation charge (Q_{CO}) derived from the CO-stripping procedure was also used to evaluate the ECSA [44,50,51]. From our earlier work [37,49], the typical CO oxidation charge per area for polycrystalline Pt is $\sim 349 \mu\text{C}/\text{cm}^2$. This charge, along with the hydrogen adsorption/desorption value of $\sim 191 \mu\text{C}/\text{cm}^2$ [37], was used to estimate the ECSA by CO stripping and hydrogen underpotential deposition (H_{UPD}), respectively. We must note that, although evaluating the H_{UPD} area is a standard method of ECSA evaluation on Pt electrodes, H binding may be modified on Pt alloys due to electronic effects such as strain effects [37]. Fifty-nanometer Pt_xGd thin films were used to evaluate electrochemical performance and for direct comparison with the 10-nm samples. We also include reference data of 40-nm-thick pure Pt thin films for comparison. Pt_xGd samples were initially cycled from 0.0 to 1.0 V vs. RHE in N_2 -saturated 0.1-M HClO_4 at 200 mV/s and 400 rpm until CVs were stable. The base CVs at 50 mV/s were then gathered at 400 rpm. The ORR activity was evaluated in O_2 -saturated electrolyte at 1600 rpm. The samples were subjected to electrochemical impedance spectroscopy (EIS) and Ohmic drop was evaluated at double-layer region at 0.5 V vs. RHE. The Ohmic drop was evaluated by linear regression of the resulting Nyquist plot in the 60 to 400 Hz region [37]. All electrochemical data in this work were presented using a Pt counter electrode and plotted relative to RHE. The RHE potential was evaluated by bubbling H_2 while rotating the working electrode at 1600 rpm and cycling between -0.74 and -0.70 V vs. the $\text{Hg}_{(l)}|\text{HgSO}_{4(g)}$ reference electrode (Schott Instruments, 0.6-M K_2SO_4). The value of the RHE potential can be read as the intercept with the current axes [37]. Finally, a base CV in N_2 -saturated electrolyte at 50 mV/s and CO-stripping CVs at 10 mV/s were obtained. Accelerated stability tests (AST) were also conducted, consisting of additional 10,000 cycles in O_2 -saturated electrolyte between 0.6 and 1.0 V vs. RHE at 100 mV/s without any electrode rotation [52]. After this extended cycling, the electrolyte was changed to a fresh one and the earlier described characterization steps were repeated.

3.3. X-ray Absorption Spectroscopy Measurements

XAS experiments were carried out ex situ at SSRL (Stanford Synchrotron Radiation Lightsource, CA, USA). Both as prepared and electrochemically conditioned samples, were transferred under ambient conditions in a sample holder. EXAFS measurements were carried out with a grazing incidence of 2° (unless otherwise stated) at beam line 11–2 at Stanford Synchrotron Radiation Lightsource (SSRL). Spectra were obtained of both Pt L_3 and Gd L_3 edges and fitted in R -space using a k^2 -weighing, see Figure 3 and supporting information (S.I.). The spectra were processed and fitted using the software package SIXPack (v1.40, SAMware, Stanford, CA, USA, 2016), using scattering paths from FEFF8 [53].

4. Conclusions

Thin film Pt_xGd electrocatalysts with different stoichiometry were fabricated using a co-sputter-deposition technique. Both 50 nm Pt_5Gd and $\text{Pt}_{7.5}\text{Gd}$ thin films are highly active catalysts for ORR. The increased activity compared to pure Pt and the difference in activity between Pt_5Gd and $\text{Pt}_{7.5}\text{Gd}$ can be explained by the inherent effect of overlayer strain. This was observed using 10-nm-thick thin film equivalents by EXAFS. We were able to detect compressive strain in the thin films and reveal that the overlayer on Pt_5Gd is more compressively strained, in good agreement with ORR activity measurements on Pt_xGd nanoparticles [21] and Pt_5Gd extended surfaces [22,31,35]. Although ORR experiments were carried out on 50-nm films and EXAFS measurements were performed on 10-nm thin films, the compressive strain values from EXAFS can be used to explain the differences in

ORR activity between Pt₅Gd and Pt_{7.5}Gd thin films. Using EXAFS, it is revealed that the overlayer on Pt₅Gd is more compressively strained than on Pt_{7.5}Gd. The powerful approach of using EXAFS to screen surface strain and thus optimal ORR response is relevant for a wide degree of Pt-alloy systems. We envisage that such flexible systems combined with powerful synchrotron analysis may open up for new avenues for electrocatalysis research.

Supplementary Materials: The following are available online at <http://www.mdpi.com/2073-4344/10/9/978/s1>, Tables S1–S7: EXAFS fitting data. Figures S1–S2: k^2 -weighted EXAFS data. Figure S3: CO stripping data normalized. Figure S4: SEM micrographs of thin films.

Author Contributions: M.E.-E., I.C. and I.E.L.S. conceived the work and designed the experiments. K.D.J. performed and analysed the electrochemical measurements and prepared the figures for the manuscript. A.F.P. acquired and analysed the X-ray absorption data. E.Z. carried out the majority of the electrochemical measurements and the thin-films fabrication. K.D.J. and M.E.-E. wrote the first draft of the paper. All authors have read and agreed to the published version of the manuscript.

Funding: We gratefully acknowledge funding for this work through the Villum Foundation V-SUSTAIN grant 9455 for the Villum Center for the Science of Sustainable Fuels and Chemicals. M.E.-E. gratefully acknowledges the Danish Council for Independent Research under the Sapere Aude– Research Talent Program and DFF-Research Project 1 (grant 9041–00224B). A.F.P. acknowledges the Danish Ministry for Higher Education and Science for an EliteForsk. K.D.J. gratefully acknowledges funding from KDFuelcell. The use of the SSRL at SLAC National Accelerator Laboratory is supported by the U.S. Department of Energy, Office of Science, Office of Basic Energy Sciences under Contract no. DE-AC02-76SF00515.

Acknowledgments: We would like to thank Apurva Mehta for assisting with synchrotron data acquisition and processing.

Conflicts of Interest: The authors declare no conflict of interest.

References

1. Debe, M.K. Electrocatalyst approaches and challenges for automotive fuel cells. *Nature* **2012**, *486*, 43–51. [[CrossRef](#)] [[PubMed](#)]
2. Kongkanand, A.; Mathias, M.F. The Priority and Challenge of High-Power Performance of Low-Platinum Proton-Exchange Membrane Fuel Cells. *J. Phys. Chem. Lett.* **2016**, *7*, 1127–1137. [[CrossRef](#)] [[PubMed](#)]
3. Vesborg, P.C.K.; Jaramillo, T.F. Addressing the terawatt challenge: Scalability in the supply of chemical elements for renewable energy. *RSC Adv.* **2012**, *2*, 7933. [[CrossRef](#)]
4. Lv, H.; Li, D.; Strmcnik, D.; Paulikas, A.P.; Markovic, N.M.; Stamenkovic, V.R. Recent advances in the design of tailored nanomaterials for efficient oxygen reduction reaction. *Nano Energy* **2016**, *29*, 149–165. [[CrossRef](#)]
5. Janik, M.J.; Taylor, C.D.; Neurock, M. First-Principles Analysis of the Initial Electroreduction Steps of Oxygen over Pt(111). *J. Electrochem. Soc.* **2009**, *156*, B126. [[CrossRef](#)]
6. Strasser, P.; Koh, S.; Anniyev, T.; Greeley, J.; More, K.; Yu, C.; Liu, Z.; Kaya, S.; Nordlund, D.; Ogasawara, H.; et al. Lattice-strain control of the activity in dealloyed core–shell fuel cell catalysts. *Nat. Chem.* **2010**, *2*, 454–460. [[CrossRef](#)]
7. Li, M.; Zhao, Z.; Cheng, T.; Fortunelli, A.; Chen, C.; Yu, R.; Zhang, Q.; Gu, L.; Merinov, B.V.; Lin, Z.; et al. Ultrafine jagged platinum nanowires enable ultrahigh mass activity for the oxygen reduction reaction. *Science* **2016**, *354*, 1414–1419. [[CrossRef](#)]
8. Mezzavilla, S.; Cherevko, S.; Baldizzone, C.; Pizzutilo, E.; Polymeros, G.; Mayrhofer, K.J.J. Experimental Methodologies to Understand Degradation of Nanostructured Electrocatalysts for PEM Fuel Cells: Advances and Opportunities. *ChemElectroChem* **2016**, *3*, 1524–1536. [[CrossRef](#)]
9. Hernandez-Fernandez, P.; Masini, F.; McCarthy, D.N.; Strebler, C.E.; Friebel, D.; Deiana, D.; Malacrida, P.; Nierhoff, A.; Bodin, A.; Wise, A.M.; et al. Mass-selected nanoparticles of Pt_xY as model catalysts for oxygen electroreduction. *Nat. Chem.* **2014**, *6*, 732–738. [[CrossRef](#)]
10. Chen, C.; Kang, Y.; Huo, Z.; Zhu, Z.; Huang, W.; Xin, H.L.; Snyder, J.D.; Li, D.; Herron, J.A.; Mavrikakis, M.; et al. Highly Crystalline Multimetallic Nanoframes with Three-Dimensional Electrocatalytic Surfaces. *Science* **2014**, *343*, 1339–1343. [[CrossRef](#)]
11. Liu, J.; Jiao, M.; Lu, L.; Barkholtz, H.M.; Li, Y.; Jiang, L.; Wu, Z.; Liu, D.J.; Zhuang, L.; Ma, C.; et al. High performance platinum single atom electrocatalyst for oxygen reduction reaction. *Nat. Commun.* **2017**, *8*, 1–9. [[CrossRef](#)]

12. Busch, M.; Halck, N.B.; Kramm, U.I.; Siahrostami, S.; Krtil, P.; Rossmeisl, J. Beyond the top of the volcano?—A unified approach to electrocatalytic oxygen reduction and oxygen evolution. *Nano Energy* **2016**, *29*, 126–135. [[CrossRef](#)]
13. Nørskov, J.K.; Rossmeisl, J.; Logadottir, A.; Lindqvist, L.; Kitchin, J.R.; Bligaard, T.; Jónsson, H. Origin of the Overpotential for Oxygen Reduction at a Fuel-Cell Cathode. *J. Phys. Chem. B* **2004**, *108*, 17886–17892. [[CrossRef](#)]
14. Stamenkovic, V.; Mun, B.S.; Mayrhofer, K.J.J.; Ross, P.N.; Markovic, N.M.; Rossmeisl, J.; Greeley, J.; Nørskov, J.K. Changing the Activity of Electrocatalysts for Oxygen Reduction by Tuning the Surface Electronic Structure. *Angew. Chem.* **2006**, *118*, 2963–2967. [[CrossRef](#)]
15. Stamenkovic, V.R.; Fowler, B.; Mun, B.S.; Wang, G.; Ross, P.N.; Lucas, C.A.; Markovic, N.M. Improved Oxygen Reduction Activity on Pt₃Ni(111) via Increased Surface Site Availability. *Science* **2007**, *315*, 493–497. [[CrossRef](#)]
16. Stephens, I.E.L.; Bondarenko, A.S.; Perez-Alonso, F.J.; Calle-Vallejo, F.; Bech, L.; Johansson, T.P.; Jepsen, A.K.; Frydendal, R.; Knudsen, B.P.; Rossmeisl, J.; et al. Tuning the Activity of Pt(111) for Oxygen Electroreduction by Subsurface Alloying. *J. Am. Chem. Soc.* **2011**, *133*, 5485–5491. [[CrossRef](#)]
17. Jensen, K.D.; Tymoczko, J.; Rossmeisl, J.; Bandarenka, A.S.; Chorkendorff, I.; Escudero-Escribano, M.; Stephens, I.E.L. Elucidation of the Oxygen Reduction Volcano in Alkaline Media using a Copper-Platinum(111) Alloy. *Angew. Chemie Int. Ed.* **2018**, *57*, 2800–2805. [[CrossRef](#)]
18. Strmcnik, D.; Escudero-Escribano, M.; Kodama, K.; Stamenkovic, V.R.; Cuesta, A.; Marković, N.M. Enhanced electrocatalysis of the oxygen reduction reaction based on patterning of platinum surfaces with cyanide. *Nat. Chem.* **2010**, *2*, 880–885. [[CrossRef](#)]
19. Escudero-Escribano, M.; Jensen, K.D.; Jensen, A.W. Recent advances in bimetallic electrocatalysts for oxygen reduction: Design principles, structure-function relations and active phase elucidation. *Curr. Opin. Electrochem.* **2018**, *8*, 135–146. [[CrossRef](#)]
20. Escudero-Escribano, M.; Verdager-Casadevall, A.; Malacrida, P.; Grønbjerg, U.; Knudsen, B.P.; Jepsen, A.K.; Rossmeisl, J.; Stephens, I.E.L.; Chorkendorff, I. Pt₅Gd as a Highly Active and Stable Catalyst for Oxygen Electroreduction. *J. Am. Chem. Soc.* **2012**, *134*, 16476–16479. [[CrossRef](#)]
21. Velázquez-Palenzuela, A.; Masini, F.; Pedersen, A.F.; Escudero-Escribano, M.; Deiana, D.; Malacrida, P.; Hansen, T.W.; Friebel, D.; Nilsson, A.; Stephens, I.E.L.; et al. The enhanced activity of mass-selected Pt_xGd nanoparticles for oxygen electroreduction. *J. Catal.* **2015**, *328*, 297–307. [[CrossRef](#)]
22. Escudero-Escribano, M.; Malacrida, P.; Hansen, M.H.; Vej-Hansen, U.G.; Velázquez-Palenzuela, A.; Tripkovic, V.; Schiøtz, J.; Rossmeisl, J.; Stephens, I.E.L.; Chorkendorff, I. Tuning the activity of Pt alloy electrocatalysts by means of the lanthanide contraction. *Science* **2016**, *352*, 73–76. [[CrossRef](#)] [[PubMed](#)]
23. Calle-Vallejo, F.; Tymoczko, J.; Colic, V.; Vu, Q.H.; Pohl, M.D.; Morgenstern, K.; Loffreda, D.; Sautet, P.; Schuhmann, W.; Bandarenka, A.S. Finding optimal surface sites on heterogeneous catalysts by counting nearest neighbors. *Science* **2015**, *350*, 185–189. [[CrossRef](#)]
24. Perez-Alonso, F.J.; McCarthy, D.N.; Nierhoff, A.; Hernandez-Fernandez, P.; Strebel, C.; Stephens, I.E.L.; Nielsen, J.H.; Chorkendorff, I. The effect of size on the oxygen electroreduction activity of mass-selected platinum nanoparticles. *Angew. Chemie Int. Ed.* **2012**, *51*, 4641–4643. [[CrossRef](#)] [[PubMed](#)]
25. Nesselberger, M.; Roefzaad, M.; Fayçal Hamou, R.; Ulrich Biedermann, P.; Schweinberger, F.F.; Kunz, S.; Schloegl, K.; Wiberg, G.K.H.; Ashton, S.; Heiz, U.; et al. The effect of particle proximity on the oxygen reduction rate of size-selected platinum clusters. *Nat. Mater.* **2013**, *12*, 919–924. [[CrossRef](#)]
26. Bu, L.; Zhang, N.; Guo, S.; Zhang, X.; Li, J.; Yao, J.; Wu, T.; Lu, G.; Ma, J.-Y.; Su, D.; et al. Biaxially strained PtPb/Pt core/shell nanoplate boosts oxygen reduction catalysis. *Science* **2016**, *354*. [[CrossRef](#)]
27. Luo, F.; Roy, A.; Silvoli, L.; Cullen, D.A.; Zitolo, A.; Sougrati, M.T.; Oguz, I.C.; Mineva, T.; Teschner, D.; Wagner, S.; et al. P-block single-metal-site tin/nitrogen-doped carbon fuel cell cathode catalyst for oxygen reduction reaction. *Nat. Mater.* **2020**. accepted. [[CrossRef](#)]
28. Jiao, L.; Zhang, R.; Wan, G.; Yang, W.; Wan, X.; Yu, S.; Jiang, H. Nanocasting SiO₂ into metalloorganic frameworks imparts dual protection to high-loading Fe single-atom electrocatalysts. *Nat. Commun.* **2020**, 1–7. [[CrossRef](#)]
29. Wan, H.; Jensen, A.; Escudero-Escribano, M.; Rossmeisl, J. Insights in the Oxygen Reduction Reaction: From Metallic Electrocatalysts to Diporphyrines. *ACS Catal.* **2020**, *10*, 5979–5989. [[CrossRef](#)]

30. Elmas, S.; Beelders, W.; Bradley, S.J.; Kroon, R.; Laufersky, G.; Andersson, M.; Nann, T. Platinum Terpyridine Metallopolymer Electrode as Cost-Effective Replacement for Bulk Platinum Catalysts in Oxygen Reduction Reaction and Hydrogen Evolution Reaction. *ACS Sustain. Chem. Eng.* **2017**, *5*, 10206–10214. [[CrossRef](#)]
31. Pedersen, A.F.; Ulrikkeholm, E.T.; Escudero-Escribano, M.; Johansson, T.P.; Malacrida, P.; Pedersen, C.M.; Hansen, M.H.; Jensen, K.D.; Rossmeisl, J.; Friebel, D.; et al. Probing the nanoscale structure of the catalytically active overlayer on Pt alloys with rare earths. *Nano Energy* **2016**, *29*, 249–260. [[CrossRef](#)]
32. Greeley, J.; Stephens, I.E.L.; Bondarenko, A.S.; Johansson, T.P.; Hansen, H.A.; Jaramillo, T.F.; Rossmeisl, J.; Chorkendorff, I.; Nørskov, J.K. Alloys of platinum and early transition metals as oxygen reduction electrocatalysts. *Nat. Chem.* **2009**, *1*, 552–556. [[CrossRef](#)]
33. Vej-Hansen, U.G.; Rossmeisl, J.; Stephens, I.E.L.; Schiøtz, J. Correlation between diffusion barriers and alloying energy in binary alloys. *Phys. Chem. Chem. Phys.* **2016**, *18*, 3302–3307. [[CrossRef](#)] [[PubMed](#)]
34. Kitchin, J.R.; Nørskov, J.K.; Barteau, M.A.; Chen, J.G. Role of Strain and Ligand Effects in the Modification of the Electronic and Chemical Properties of Bimetallic Surfaces. *Phys. Rev. Lett.* **2004**, *93*, 156801. [[CrossRef](#)] [[PubMed](#)]
35. Escudero-Escribano, M.; Pedersen, A.F.; Ulrikkeholm, E.T.; Jensen, K.D.; Hansen, M.H.; Rossmeisl, J.; Stephens, I.E.L.; Chorkendorff, I. Active-Phase Formation and Stability of Gd/Pt(111) Electrocatalysts for Oxygen Reduction: An In Situ Grazing Incidence X-Ray Diffraction Study. *Chemistry* **2018**, 1–12. [[CrossRef](#)]
36. Ulrikkeholm, E.T.; Pedersen, A.F.; Vej-Hansen, U.G.; Escudero-Escribano, M.; Stephens, I.E.L.; Friebel, D.; Mehta, A.; Schiøtz, J.; Feidenhansl, R.K.; Nilsson, A.; et al. Pt x Gd alloy formation on Pt(111): Preparation and structural characterization. *Surf. Sci.* **2016**, *652*, 114–122. [[CrossRef](#)]
37. Zamburlini, E.; Jensen, K.D.; Stephens, I.E.L.; Chorkendorff, I.; Escudero-Escribano, M. Benchmarking Pt and Pt-lanthanide sputtered thin films for oxygen electroreduction: Fabrication and rotating disk electrode measurements. *Electrochim. Acta* **2017**, *247*, 708–721. [[CrossRef](#)]
38. Lindahl, N.; Zamburlini, E.; Feng, L.; Grönbeck, H.; Escudero-Escribano, M.; Stephens, I.E.L.; Chorkendorff, I.; Langhammer, C.; Wickman, B. High Specific and Mass Activity for the Oxygen Reduction Reaction for Thin Film Catalysts of Sputtered Pt3Y. *Adv. Mater. Interfaces* **2017**, *4*, 1–9. [[CrossRef](#)]
39. Lindahl, N.; Eriksson, B.; Grönbeck, H.; Lindström, R.W.; Lindbergh, G.; Lagergren, C.; Wickman, B. Fuel Cell Measurements with Cathode Catalysts of Sputtered Pt3Y Thin Films. *ChemSusChem* **2018**, *11*, 1438–1445. [[CrossRef](#)]
40. Bandarenka, A.S.; Hansen, H.A.; Rossmeisl, J.; Stephens, I.E.L. Elucidating the activity of stepped Pt single crystals for oxygen reduction. *Phys. Chem. Chem. Phys.* **2014**, *16*, 13625. [[CrossRef](#)]
41. Marković, N.M.; Gasteiger, H.A.; Ross, P.N., Jr. Oxygen Reduction on Platinum Low-Index Single-Crystal Surfaces in Sulfuric Acid Solution: Rotating Ring-Pt(hkZ) Disk Studies. *J. Phys. Chem.* **1995**, *99*, 3411. [[CrossRef](#)]
42. López-Cudero, A.; Cuesta, A.; Gutiérrez, C. Potential dependence of the saturation CO coverage of Pt electrodes: The origin of the pre-peak in CO-stripping voltammograms. Part 1: Pt(111). *J. Electroanal. Chem.* **2005**, *579*, 1–12. [[CrossRef](#)]
43. McCarthy, D.N.; Strebler, C.E.; Johansson, T.P.; den Dunnen, A.; Nierhoff, A.; Nielsen, J.H.; Chorkendorff, I. Structural Modification of Platinum Model Systems under High Pressure CO Annealing. *J. Phys. Chem. C* **2012**, *116*, 15353–15360. [[CrossRef](#)]
44. Lebedeva, N.P.; Koper, M.T.M.; Feliu, J.M.; Van Santen, R.A. Role of crystalline defects in electrocatalysis: Mechanism and kinetics of CO adlayer oxidation on stepped platinum electrodes. *J. Phys. Chem. B* **2002**, *106*, 12938–12947. [[CrossRef](#)]
45. Bard, A.J.; Faulkner, L.R. *Electrochemical Methods: Fundamentals and Application*, 2nd ed.; Wiley: New York, NY, USA, 2001; ISBN 0471043729.
46. Marković, N.M.; Ross, P.N., Jr. Surface science studies of model fuel cell electrocatalysts. *Surf. Sci. Rep.* **2002**, *45*, 117–229. [[CrossRef](#)]
47. Rudi, S.; Cui, C.; Gan, L.; Strasser, P. Comparative Study of the Electrocatalytically Active Surface Areas (ECSAs) of Pt Alloy Nanoparticles Evaluated by Hupd and CO-stripping voltammetry. *Electrocatalysis* **2014**, *5*, 408–418. [[CrossRef](#)]
48. Biegler, T.; Rand, D.A.J.; Woods, R. Limiting oxygen coverage on platinized platinum; Relevance to determination of real platinum area by hydrogen adsorption. *J. Electroanal. Chem.* **1971**, *29*, 269–277. [[CrossRef](#)]

49. Pedersen, C.M.; Escudero-Escribano, M.; Velázquez-Palenzuela, A.; Christensen, L.H.; Chorkendorff, I.; Stephens, I.E.L. Benchmarking Pt-based electrocatalysts for low temperature fuel cell reactions with the rotating disk electrode: Oxygen reduction and hydrogen oxidation in the presence of CO (review article). *Electrochim. Acta* **2015**, *179*, 647–657. [[CrossRef](#)]
50. García, G.; Koper, M.T.M. Carbon Monoxide Oxidation on Pt Single Crystal Electrodes: Understanding the Catalysis for Low Temperature Fuel Cells. *ChemPhysChem* **2011**, *12*, 2064–2072. [[CrossRef](#)]
51. Weaver, M.J.; Chang, S.C.; Leung, L.W.H.; Jiang, X.; Rubel, M.; Szklarczyk, M.; Zurawski, D.; Wieckowski, A. Evaluation of absolute saturation coverages of carbon monoxide on ordered low-index platinum and rhodium electrodes. *J. Electroanal. Chem.* **1992**, *327*, 247–260. [[CrossRef](#)]
52. Ohma, A.; Shinohara, K.; Iiyama, A.; Yoshida, T.; Daimaru, A. Membrane and Catalyst Performance Targets for Automotive Fuel Cells by FCCJ Membrane, Catalyst, MEA WG. *ECS Trans.* **2011**, *41*, 775–784. [[CrossRef](#)]
53. Rehr, J.J.; Albers, R.C. Theoretical approaches to x-ray absorption fine structure. *Rev. Mod. Phys.* **2000**, *72*, 621–654. [[CrossRef](#)]



© 2020 by the authors. Licensee MDPI, Basel, Switzerland. This article is an open access article distributed under the terms and conditions of the Creative Commons Attribution (CC BY) license (<http://creativecommons.org/licenses/by/4.0/>).